PHYSICAL REVIEW B VOLUME 30, NUMBER 9 1 NOVEMBER 1984

Damping of second sound near the superfluid transition of ^{4}He as a function of pressure

Raui Mehrotra* and Guenter Ahlers
Department of Physics, University of California, Santa Barbara, California 93106

(Received 7 May 1984)

Quantitative experimental results of the second-sound damping D_2 near the superfluid transition temperature $T_\lambda(P)$ are presented at several pressures P as a function of the reduced temperature $t=1-T/T_\lambda(P)$. The data cover the entire pressure range of the transition and are for $2\times10^{-5}\lesssim t\lesssim0.1$. Their experimental uncertainty is in the range of 2–4 %. The experimental technique used in this work is described in detail. It is based on a tone-burst method and includes a number of novel features such as discrimination against higher harmonics by spectral analysis of the pulses, rectification before signal averaging to avoid the detrimental effect of temperature noise, a careful study of finite-amplitude effects, and quantitative corrections for nonparallelism of the cavity ends. The results are compared with the predictions based on renormalization-group theory and thermal-conductivity measurements above T_λ. The intricate pressure dependence of the data, which changes sign near $t\approx10^{-3}$, is given rather well by the prediction. However, the details of the temperature dependence of the data at a given pressure disagree with the theory in its present form by deviations somewhat greater than the experimental uncertainty.

I. INTRODUCTION

The study of the dynamics of the superfluid transition of ^{4}He has been actively pursued for very many years, and a number of recent reviews, written from various viewpoints, describe it in some detail.[1–5] Nonetheless, before proceeding to a discussion of our experiments, we would like to outline briefly, from our point of view, the major events that have motivated us to undertake the present work.

Nearly two decades ago, the thermal-conductivity measurements near the λ line in ^{4}He of Kerrisk and Keller,[6,7] and the simultaneously evolving theory of dynamic scaling,[8,9] demonstrated that transport coefficients may diverge near critical points. This behavior differs dramatically from that predicted by the Van Hove theory,[10] in which transport coefficients are assumed to remain finite and the diffusivities have the same singularities as the corresponding inverse thermodynamic susceptibilities. The early experimental work[6,7] was followed almost immediately by quantitative measurements of the thermal conductivity extremely close to the λ point at saturated vapor pressure[11,12] which appeared to confirm the dynamic-scaling prediction in considerable detail. These results and—even more so—somewhat later experiments at elevated pressure near the λ line[13] did raise some important quantitative questions, however, which were not readily answered by the phenomenological dynamic-scaling ideas. Their full significance was, in fact, not generally appreciated until much later. The issues raised by the data were as follows:

(1) The measured thermal conductivity could not be represented by a simple power law even for reduced temperatures t $(=|T/T_\lambda-1|)$ as small as 10^{-5}. Instead, confluent singular terms had to be used to fit the data.[13]

(2) Even when confluent singular terms were included in the data analysis, the leading exponent derived from the experiment was larger than the dynamic-scaling prediction by about 0.06.[13]

(3) The critical region in which the thermal conductivity rises appreciably above its background (high-temperature) value is two decades narrower $(t\lesssim10^{-3})$ than it is for the static properties $(t\lesssim10^{-1})$.[11–13]

(4) The thermal conductivity had a strong dependence upon the cell height h even for h much larger than the correlation length ξ.[11]

All except the last of these issues are now understood quantitatively on the basis of an application to transport properties[14,15] of the renormalization-group theory of critical phenomena.[16] Detailed calculations[14,17–19] within the framework of this theory made it clear that an expansion of the theoretical prediction in terms of the usual power laws ceases to be meaningful in this case because of the existence of extremely slow transients.[18,20–22] These transients explain experimental observations (1) and (2) above. It was recognized by Hohenberg, Halperin, and Nelson,[22] and independently by Dohm and Folk,[23] that a quantitative comparison between theory and experiment was possible nonetheless. These authors proposed a numerical integration of the renormalization-group recursion relations[18,19] in which the initial values for the integration at some arbitrarily chosen reference temperature are adjusted until a fit to the measurements is obtained. Such an analysis was first performed by Dohm and Folk[23,24] initially using the symmetric planar spin model (model E) of Halperin *et al.*[14] Model E is expected to represent the dynamics of liquid helium only approximately and does not accurately contain the coupling of the specific heat to the order parameter. An analysis in terms of the more appropriate asymmetric model F (Ref. 14) was presented soon thereafter by Ahlers, Hohenberg, and Kornblit,[25] and by Dohm and Folk.[26] Model F is expected to reproduce

©1984 The American Physical Society

the dynamics of this transition exactly. The comparison between experiment and theory[23–26] has revealed quantitative agreement in spite of the complicated dynamics near this transition. It has also demonstrated that the narrow critical region for the dynamics [point (3) above] is a natural consequence of an anomalously small, bare dynamic coupling constant for liquid helium.[25] (For a discussion of some of these points, also see the work of Ferrell and Bhattacharjee.[20,21])

The analysis of the thermal conductivity *above* T_λ fixes the nonuniversal parameters in the theory by providing the initial values of the integration of the recursion relations. This integration gives the two dynamic variables f and w as a function of t. The second-sound damping *below* T_λ, in principle, can then be obtained from f and w without any further adjustable parameters.[24] The dependence of D_2 upon f and w has been obtained by Dohm and Folk,[24,27] albeit, so far, only for model E. Combining this formula with the model-F analysis of the thermal conductivity has yielded specific predictions of D_2 at several different pressures.[25,27] Experimental measurements for D_2 exist only at saturated vapor pressure,[28–31] and even there the best data near T_λ (Ref. 30) have experimental uncertainties as large as 15–20%. This scarcity of information below T_λ is remedied to a large extent by the present work. We present measurements at several pressures up to 28 bars with experimental uncertainties in the range 2–4%. A brief report of this work has already been presented elsewhere.[32] Comparison of these experimental results with the predictions shows that the theory has been remarkably successful in reproducing the overall features of the data. Specifically, the rather intricate pressure dependence of D_2, which changes sign at a reduced temperature slightly less than 10^{-3}, is given very well. However, the *detailed* temperature dependence of the data at a given pressure is reproduced only approximately. It will be important to see if this disagreement at a quantitative level can be removed by a systematic calculation of D_2 which uses model F consistently both above and below T_λ.

More recently, a prediction of D_2 has also been obtained[33,34] from the experimental thermal conductivity[13,25] by Ferrell and Bhattacharjee.[20] This theoretical approach neglects the dissipative couplings of the dynamic modes which are associated with the coupling terms in the free energy,[35] and, therefore, we consider it to be less systematic than the calculations[24,27] based on the renormalization-group theory.[14,15] Furthermore, Ferrell and Bhattacharjee restrict their calculations to temperatures not too close to T_λ where the weak-coupling regime[25] exists for the dynamics and permits a "high-temperature" expansion. A correction in the "background" region which was added later[34] to the original prediction[33] of D_2 has been criticized recently.[36] We shall compare our experimental results to the theory with and without that correction. At vapor pressure and for $t \lesssim 10^{-3}$ the original prediction[33] is numerically not very different from that based on the renormalization-group theory, but for larger t, where this theory should be valid, it predicts a smaller D_2 and disagrees with the data by a considerable amount. To our knowledge, the theory has not yet been used to predict D_2 at higher pressures.

In the next section we describe in detail our experimental method. This includes, as crucial features to the success of the measurements, the design of bolometers an order of magnitude more sensitive than those used previously for second-sound—damping measurements,[30] careful quantitative corrections for wedging effects associated with slight departures from parallelism of the heater and bolometer, and a novel half-wave rectification technique which avoids the detrimental effect of temperature noise on signal averaging of the measurements. Also discussed are the application of spectral-analysis techniques to the measurement of echo intensities, various extraneous loss mechanisms, and finite-amplitude and bolometer-power effects. In Sec. III we present our experimental results for D_2 and compare them with previous measurements. Section IV consists of a comparison of our data with the theory. The measurements at vapor pressure are compared with the damping of first sound in Sec. V. A brief summary is provided in Sec. VI.

II. EXPERIMENTAL TECHNIQUES

A. Techniques for measuring second-sound attenuation and their relative merit

Several methods have been used to measure the attenuation of second sound. Hanson and Pellam[28] used a free traveling-wave system in which the transmitter-receiver separation could be varied. They made a direct measurement of the sound amplitude after it had traversed different distances in liquid helium. Their measurements, however, did not extend into the region $t \lesssim 10^{-2}$. Worthington *et al.*[37] measured the damping of second sound by studying the evolution of the shape of heat pulses, but their measurements were also made only for temperatures much less than T_λ. Tyson,[31] Ahlers,[29] and Crooks and Robinson[30,38] excited standing-wave resonances of second sound. While Tyson and Ahlers measured the linewidth of resonances in their experiments, Crooks and Robinson measured the time of decay of the resonances after the drive was turned off.

One disadvantage of using a resonance method is that only low-frequency resonances, which are sufficiently isolated in frequency from other resonant modes of the cavity, can be used. At low frequencies, the surface losses in the cavity are large compared to the damping in bulk helium. The uncertainty in the measured bulk damping is thus relatively large. Another disadvantage is that a large amplitude of second sound builds up in the cavity due to the high quality factor of the resonances. An extrapolation of results to small amplitudes therefore becomes necessary in the region near the λ point where nonlinear contributions to the hydrodynamics become important.

For the experiments reported in this paper we used a cylindrical cavity with a second-sound generator at one end and a detector at the other. A tone burst of second sound was generated which traversed back and forth between the ends of the cavity. The damping was determined by measuring the amplitude of the second-sound echoes at the detector. To improve the signal-to-noise ratio it was necessary to repeat the above process and average the signal over many sweeps. This technique had several advantages. When the damping was not too large we were able to use frequencies as large as 100 kHz. In that case, the bulk damping dominated extraneous losses. By improving on the bolometers reported in Ref. 38, we were able to use lower second-sound amplitudes, where the effect of finite amplitudes on the damping was negligible compared to the uncertainty in the measurements. Since no resonant excitations were involved, there was no buildup of second-sound amplitude in any part of the cavity.

Close to T_λ the temperature stability of the measuring system becomes important. The temperature fluctuations cause a significant change in the second-sound velocity. This noise makes an accurate measurement of the damping difficult when certain techniques are used. For example, the frequency of a resonance fluctuates and a true measurement of the linewidth is difficult to obtain. In the resonance-decay method used by Crooks and Robinson[30,38] it is an important advantage that the temperature noise does not affect the decay time appreciably because the amplitude of a freely decaying resonance is measured. In our method, if we average over many sweeps the temperature noise causes a fluctuation in the arrival time of the echoes at the detector. This leads to an interference between the signals received during successive sweeps, and a true measurement of the echo amplitudes cannot be made. We were able to remedy this problem and at the same time retain the advantage of the tone-burst method by averaging over a half-wave-rectified signal rather than the full signal. The details of this process are described in subsection H below.

A disadvantage of the echo method arises if the two ends of the cavity are not exactly parallel. In that case, the exponential decay pattern of the echo amplitudes is modulated by a nonexponential function of the angle between the two ends of the cavity. However, the nonexponential part can be separated out under favorable circumstances and the wedge angle can be determined from it. Thereafter, this angle can be taken into consideration in the data analysis.

B. Design of the cells

Three cells of 2.03 cm i.d. and 5.08 cm o.d. were machined out of copper. The lengths of the cells at low temperatures were 0.404, 1.225, and 3.678 cm, respectively. The cylindrical cavities were polished to increase the Kapitza resistance[39] between the walls of the cavity and the liquid helium. This helped in reducing the damping of second sound due to thermal conduction at the walls. A second-sound generator was mounted on one end of each of the cavities. Heaters made out of thin resistive films of chromium were used as generators. On the other end of each cavity a second-sound detector consisting of superconducting gold-lead composite film[38,40] was mounted. Mylar spacers, about 40 μm thick, were used to electrically isolate the heater and bolometer films from the copper body of the cells. The cavities were sealed at the ends with brass caps and indium gaskets. The leads from the heaters and bolometers were connected to hermetically sealed coaxial connectors mounted in the brass caps. The cells could be filled with liquid helium though a fill line soldered to one of the brass caps on each cell.

C. Design of heater films

The heaters were made by depositing a film of chromium, about 300 Å thick, on a glass slide. The glass slides were $2.5\times2.5\times0.32$ cm in size. They were sufficiently flat to produce only a few interference fringes across their face when placed against an optically flat surface and illuminated with yellow light. The resistance of the films was approximately 350 $\Omega/\square$. Usual vapor-deposition techniques were employed with some precautions taken to make the films uniform. The source-to-substrate distance was kept large, about 30 cm, and a line source was used as opposed to a point source. Electrical contact with the film was made by depositing strips of 300 Å of chromium and about 1500 Å of gold on top of the chromium on two edges of the glass slides. Thin copper wires were soldered to the conducting strips using indium and an ultrasonic soldering iron. The electrodes were deposited first, followed by the resistive chromium film. As shown in Fig. 1, the heater films were square in shape to make the current density, and hence the heating produced, uniform over the area of the film.

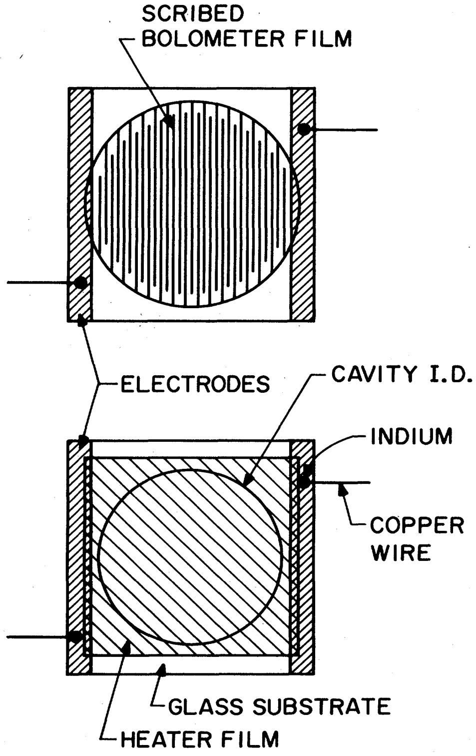

FIG. 1. Schematic diagram of the heater and bolometer. The circle on the heater film shows the position of the end of the cavity when the cell is assembled.

D. Design of bolometers

The bolometer films were deposited in a similar way as the heaters. The electrodes were deposited first. The bolometers consisted of a lead film deposited on top of a gold film. The ratio of the thickness of the lead to the gold film was 1.55. The total thickness of a bolometer film was approximately 200 Å. This thickness ratio gave a superconducting transition between 2.18 and 2.23 K. The same precautions were taken as in the case of heater films to make the bolometers uniform. In addition, since two materials, gold and lead, had to be deposited in this case, the gold was deposited first and then the gold source was replaced by a lead source in the same position instead of mounting the two sources side by side. A few hours after the deposition, the room-temperature resistance of the gold-lead films became constant and was about 30 $\Omega/\Box$.

The signal δV generated by a temperature change δT in a bolometer of resistance R is given by

$$\delta V=(PR)^{1/2}K\,\delta T\ , \tag{1}$$

where P is the power dissipated by the bias current through the bolometer, and K is the figure of merit defined by

$$K=\frac{1}{R}\frac{dR}{dT}\ . \tag{2}$$

According to Eq. (1), if the power dissipation is to be kept small, the resistance should be increased to maintain the signal level. To achieve this the bolometer films were scribed as shown in Fig. 1. This increased the room-temperature resistance of the films from about 30 Ω to about 150 kΩ. For scribing, the glass slide was mounted on a milling-machine table and moved against a fixed carbon-steel scalpel blade. The scribed lines were 25—50 μm wide and 250 μm apart. The bolometers were stored in a vacuum dessicator until ready for mounting on the cells.

The resistance of the bolometers dropped by a factor of 2 upon cooling to helium temperatures. When biased in the middle of the superconducting transition, the operating resistance of a bolometer, hence, was about a quarter of the room- temperature value, that is, about 35 kΩ. The figure of merit was measured to be 45 K^{-1}. The magnetic field required to shift the transition temperature from 2.2 K in zero field down to about 1.7 K was 700—800 G.

Second-sound signals of about 10 nK amplitude could be resolved directly with the bolometer. A resolution of 1 nK was achieved with the help of signal averaging. The limiting factor for the resolution was the Johnson noise.

E. Experimental setup

The overall experimental setup was rather simple. It consisted of three experimental cells of different lengths immersed in a liquid-helium bath. The sealed cells were filled with helium through a fill line of 0.25 mm i.d. to the required pressure and then isolated from the helium supply line and the pressure-measurement system at room temperature by closing a valve located at the top of the cryostat. The bath was pumped to the appropriate temperature. A superconducting solenoid of 30 cm length and 8.9 cm i.d. surrounded the cells and provided the magnetic field necessary to tune the transition temperature of the superconducting bolometer films in the cells to the working temperature. The superconducting magnet was operated in the persistent mode to avoid the modulation of the bolometer transition temperature by noise and ripple from the magnet current supply. Coaxial and other leads were brought down a stainless-steel tube which supported the apparatus.

The temperature of the bath was measured by monitoring the vapor pressure in the bath with the help of an MKS pressure gauge with a Baratron model 145 BHS-100 pressure head, and also by measuring the second-sound velocity.[41] The bath temperature was regulated by using a Cryocal model CR500 germanium thermometer and a reference resistor immersed in the bath and connected to an ac bridge.[42] The bridge was balanced at the working temperature. The error signal from the bridge was fed back through a Linear Research model LR-130 temperature controller to a 300-Ω resistive heater in the bath. The short-term temperature stability of this regulating system was a fraction of a micro-Kelvin. Over longer periods of time, the bath temperature drifted. Drift rates of up to 1 μK/min were observed. The major cause of the drift was the relaxation of the germanium thermometer after it was subjected to a change in the magnetic field. This drift was insignificant during the time interval in which a set of data was collected.

The pressure in the cells was measured by an MKS pressure gauge with a model 310 BH-10000 pressure head for pressures less than 13 bars. For higher pressures, the second-sound velocity[41] and the vapor pressure in the bath were used to determine the pressure inside the cells. The pressure inside the cells was not regulated. An accurate knowledge of the pressure is not required. The reduced temperature, t, is well known from measurements of u_2.

F. Electronics and procedure

A block diagram of the electronics is shown in Fig. 2. A burst of several cycles of a sine wave produced by a

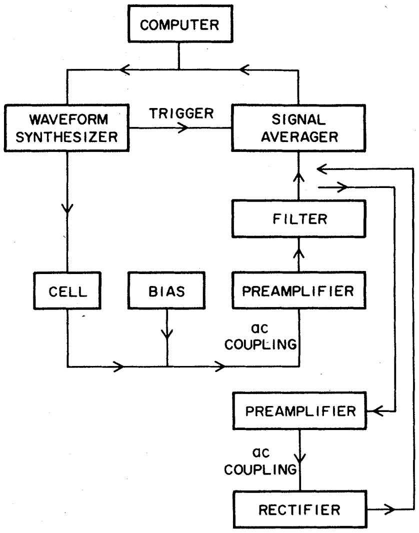

FIG. 2. Block diagram of the electronics.

Wavetek model 178 programmable waveform synthesizer at a frequency $f/2$ was applied to the heater in the cell. This produced second sound at frequency f. The bolometer was biased by a simple homemade constant-current circuit which used a battery as the source. Currents from 1–100 μA were used in the experiments. The output of the bolometer was ac coupled to a Princeton Applied Research model 113 preamplifier. The amplified output was fed to a Nicolet model 1170 signal averager through a Krohn-Hite model 3202 bandpass filter which was centered around the frequency of interest, f. The bandwidth used was approximately $0.2f$. The filter had 12 db/octave rolloff.

The signal averager was triggered by the waveform synthesizer at the time the tone burst was created. The trigger could also be delayed by a known time if desired. The averager recorded the signal received at the bolometer as a function of time in digital form in 4096 channels. The total time interval on the signal averager was adjusted according to the number of echoes to be recorded and the time resolution desired. Afer the second sound in the cavity decayed to the background-noise level, another burst of second sound was created at the heater and the process was repeated until a satisfactory signal-to-noise ratio was obtained at the signal averager. The data were then transferred from the signal averager to a Hewlett-Packard model 9845B computer for processing. The computer also controlled the waveform synthesizer.

When working close to the λ transition where the temperature noise became significant, another amplifier and a half-wave rectifier were inserted between the filter and the signal averager (see below).

At a given pressure and temperature, the echo pattern was recorded at each of several frequencies of second sound. The damping coefficient D_2 was deduced from the frequency dependence of the attenuation. The temperature was then varied to measure D_2 as a function of temperature for a fixed pressure. This process was repeated for various pressures.

G. Determination of echo intensities

Figure 3 shows a typical echo pattern obtained when no bandpass filter is used. An equivalent echo pattern is shown in Fig. 4 with the bandpass filter in place. The envelope frequency corresponding to the time interval of each echo has been filtered out. The first echo of Fig. 4 is shown in detail in Fig. 5.

To determine the intensity of each echo from such an echo pattern (not too close to the λ transition where the temperature noise was negligible), a fast Fourier transform (FFT) was performed and a power spectrum calculated for each echo. The spectrum was integrated over a small frequency range Δf around the frequency of interest f to obtain the intensity of an echo. At least 256 points in each echo consisting of several cycles at frequency f were used for the FFT. At least one cycle at the beginning and the end of each echo was discarded to eliminate the effect of transients. A typical spectrum is shown in Fig. 6. A spectrum was also calculated for the background noise (region between two echoes in Fig. 4). The noise at frequency f has no fixed phase relationship with the signal at frequency f. Hence, the intensities of the signal and the noise, rather than the amplitudes, are additive. Thus the noise intensity at f was subtracted from the intensity of each echo. This correction was usually negligible.

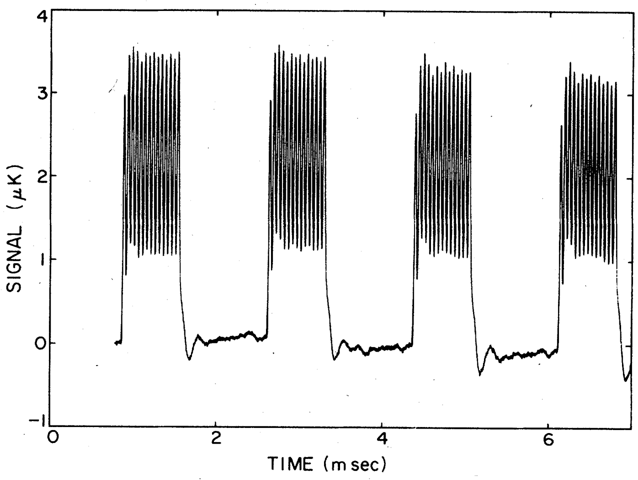

FIG. 3. Typical echo pattern obtained at vapor pressure far below T_λ in the medium-length cell without the bandpass filter. 64 sweeps were averaged. The lower and upper frequency rolloff points for the preamplifier were 1Hz and 300 kHz, respectively. For this run, $u_2=1399$ cm/sec, corresponding to $t=0.05$. The frequency was 20 kHz.

No harmonics of the second-sound frequency were present in the spectra of echoes (Fig. 6). A spectrum of echoes from an echo pattern recorded without the use of a filter (see Fig. 3, for example) also showed no harmonics. Thus, the filter was important only to limit the bandwidth and thereby to reduce noise. The absence of harmonics was important when a rectifier circuit was used for measurements close to the λ point. This is discussed in the next section.

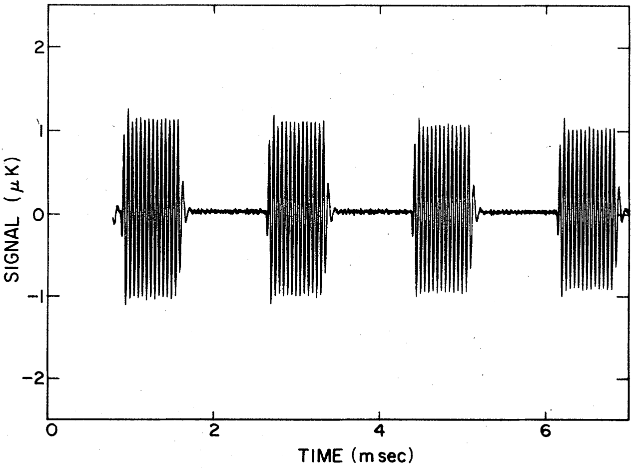

FIG. 4. Same echo pattern as in Fig. 3 with the bandpass filter centered at 20 kHz and the bandwidth at 10 kHz.

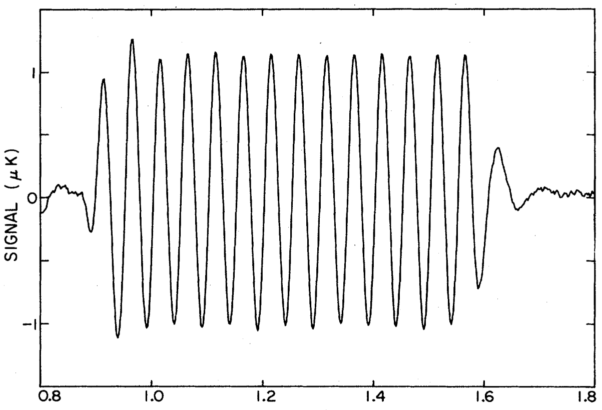

FIG. 5. Expanded plot of the first echo shown in Fig. 4.

H. Use of the rectifier circuit

Near T_λ, where the temperature noise is significant, there may be a phase difference between the signals at frequency f received in two different sweeps. The phase difference $\delta\phi$ is given by

$$\delta\phi = 2\pi f\,\delta\tau\ , \tag{3}$$

where

$$\tau = (2n-1)l/u_2 \tag{4}$$

is the arrival time of the nth echo, and l is the length of the cell. The second-sound velocity depends on the temperature T and thus introduces temperature noise into the phase. The above equations ignore the high-frequency temperature fluctuations occurring within the arrival period of a particular echo. Combining Eqs. (3) and (4), one has

$$\delta\phi = -\frac{2\pi(2n-1)lf}{u_2}\frac{d(\ln u_2)}{dT}\delta T\ . \tag{5}$$

For a sufficiently large number of averaged samples, the signal from the fundamental frequency contained in the nth echo is well approximated by

$$\bar{S}_n = \bar{A}_{n1}\cos(\omega t)\ , \tag{6}$$

with

$$\bar{A}_{n1} = A_{n1}\int_{-\infty}^{\infty} g(\phi)\cos\phi\, d\phi\ . \tag{7}$$

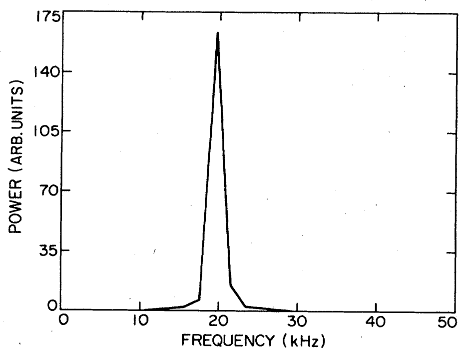

FIG. 6. Power spectrum of the first echo shown in Fig. 4.

Here, A_{n1} is the amplitude of the fundamental frequency component of the nth echo in the absence of noise. The function $g(\phi)$ is the normalized-phase noise distribution and is related to the temperature noise distribution by Eq. (5). In obtaining Eq. (7) we have assumed $g(\phi)$ to be symmetric about $\phi=0$. As an example, consider the Gaussian distribution

$$g(\phi) = (\beta/\pi^{1/2})e^{-\beta^2\phi^2}\ . \tag{8}$$

For that case,

$$\bar{A}_{n1} = A_{n1}\exp\left[-\frac{1}{4\beta^2}\right]\ . \tag{9}$$

According to Eq. (5), β^{-1} is proportional to $2n-1$. Hence, the later echoes, i.e., echoes with larger n, are affected more by the temperature noise.

In principle, the function $g(\phi)$ can be measured and the echo amplitudes corrected, but in practice $g(\phi)$ is a function of the bath temperature and the amount of helium in the bath. Hence, a measurement of $g(\phi)$ is impractical.

An easier way to remedy the situation is by averaging over the squares of the signals from many samples rather than the amplitude. In that case, the average of intensity of an echo $\bar{I} = \overline{S^2}$ is given by

$$\bar{I} = \bar{I}_0 + \bar{I}_1\cos(2\omega t)\ , \tag{10a}$$

with

$$\bar{I}_0 = \tfrac{1}{2}A_{n1}^2 \tag{10b}$$

and

$$\bar{I}_1 = \tfrac{1}{2}A_{n1}^2\int_{-\infty}^{\infty} g(\phi)\cos(2\phi)d\phi\ . \tag{10c}$$

Thus the amplitude A_{n1} is contained in the zero-frequency component of the spectrum of $\bar{I}$, and therefore is given also by

$$A_{n1}^2 = 2\langle \bar{I}\rangle\ , \tag{11}$$

where $\langle \bar{I}\rangle$ is the mean of $\bar{I}$. Thus, the determination of A_{n1} by this method is not sensitive to phase (or temperature) noise.

Experimentally, the above procedure would require a squaring amplifier inserted before the signal averager. Alternately, the amplitudes A_{n1} can be determined by using an absolute-value circuit and averaging over the absolute value of the signal. In this case,

$$A_{n1} = \frac{2}{\pi}\langle\, |S|_{\rm av}\rangle\ , \tag{12}$$

where $\langle\, |S|_{\rm av}\rangle$ is the mean of $|S|_{\rm av}$, the average of the absolute value of the signal.

The signal averager used in the experiments did not have a highly stable dc offset. Hence the use of a squaring amplifier or an absolute-value circuit would give intensities of echoes offset by an unknown amount. To eliminate this problem, a precision homemade half-wave rectifier was used. A typical echo pattern is shown in Fig. 7(a). The signal arriving before the first echo is the pick-

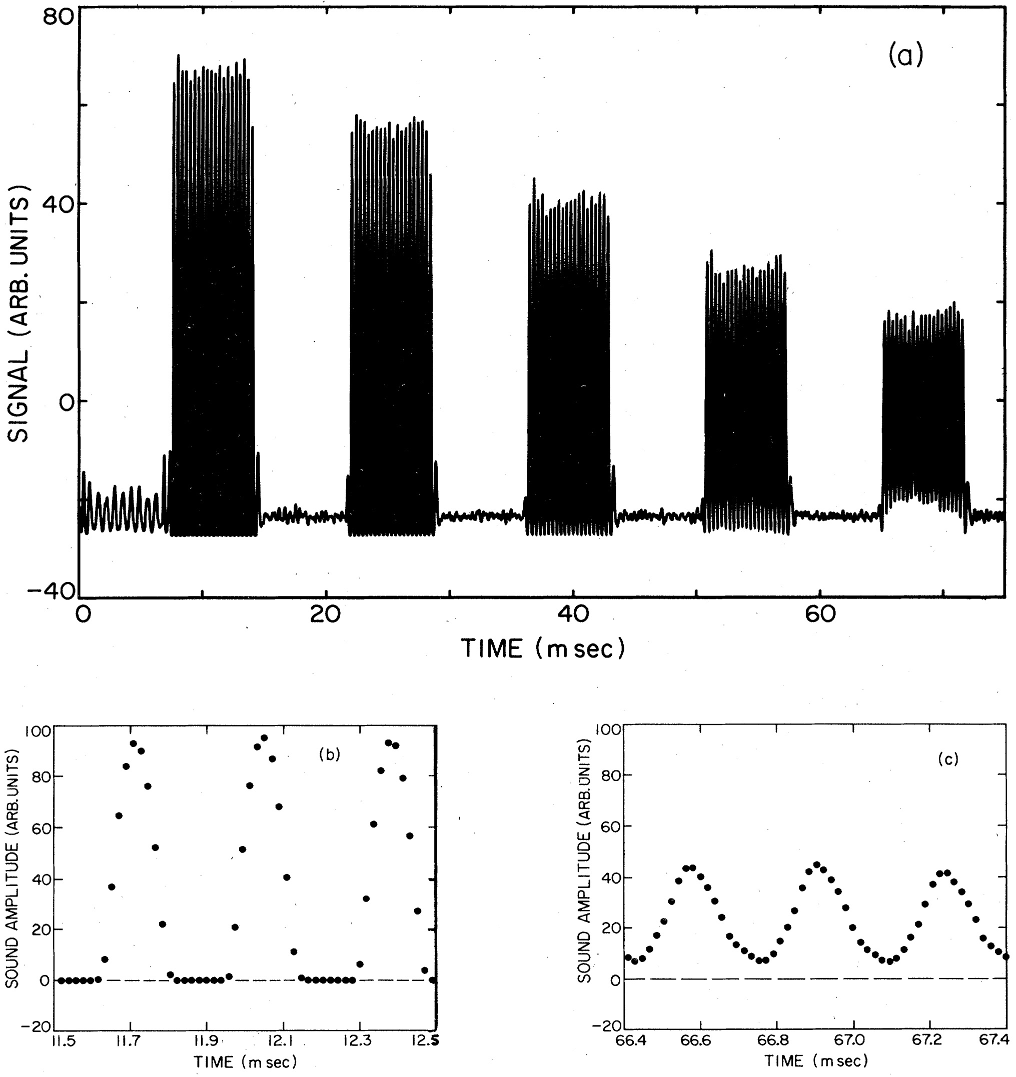

FIG. 7. (a) Typical echo pattern obtained at vapor pressure and near T_λ in the medium-length cell with the half-wave rectifier in place. 100 sweeps were averaged. For this run $u_2=170$ cm/sec, corresponding to $t=2\times10^{-4}$. The frequency was 3 kHz. (b) Exploded view of the contents of the first echo in (a). (c) Exploded view of the contents of the fifth echo in (a).

up at frequency $f/2$ which is small in amplitude because of the bandpass filter in the circuit. An exploded view of part of the first and the fifth echoes is shown in Figs. 7(b) and 7(c), respectively. Since the effect of noise on the first echo is small, the averaged signal during the first echo, when the rectifier was nonconducting, fixed the zero level.

Once the zero level was fixed as described above, a number of points (256, for convenience) was selected within each echo. Again, at least one cycle in the beginning and the end of each echo was discarded. The mean of these points gave A_{n1}/π. The same procedure was used to determine the background by selecting points between two echoes. The background intensity was subtracted from the echo intensities.

To determine the attenuation for a single frequency f, it was important that no harmonics of the second-sound frequency were present in the signal because no frequencies were discriminated against in averaging over $|S|$. As seen from the Fourier spectra of echoes, no such harmonics were present. In case they were present, the filter would have filtered them out.

I. Wedging effects and determination of attenuation coefficient

Once the echo intensities are obtained as described above, it should be a straightforward procedure to fit the intensities to an exponential decay curve to determine the attenuation coefficient. However, in the measurement technique used, "wedging effects" cause a nonexponential decay which must be taken into account.

The signal obtained from a bolometer is the integrated response to temperature variations over its area. For this reason, if there are phase variations across the area of the bolometer, interference takes place. In the measurement technique used, different parts of the second-sound plane-wave front travel different distances if the heater and the bolometer deviate from parallelism by an angle θ. This leads to phase variations of the temperature wave reaching the bolometer. The interference causes a modulation of the echo amplitudes by a function $F(\theta)$, which, in the absence of walls around the cavity, is given by[43]

$$F(\theta)=2J_1(y)/y \ , \tag{13a}$$

with

$$y=\frac{r}{l}\theta\omega\tau \ . \tag{13b}$$

Here, J_1 is the Bessel function of order 1, r is the cavity radius, and τ is the time measured from the instant when the heater is activated. The function F is plotted in Fig. 8.

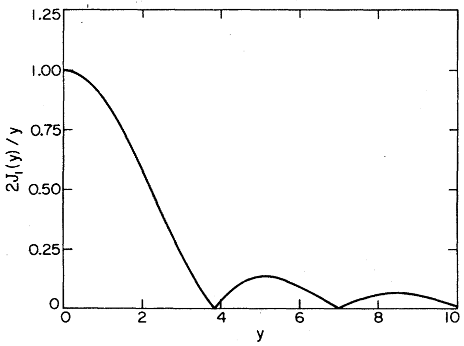

FIG. 8. Modulation function for the echo amplitudes in a wedged sample.

In the presence of walls the modulation will not deviate appreciably from Eqs. (13) until a time when a significant portion of the wavefront is reflected from the walls. Hence, for small values of θ the intensity of a large number of echoes can be fitted by the function

$$I_n=I_0\exp(-2\alpha x_n)\left[\frac{2J_1(y_n)}{y_n}\right]^2 , \tag{14}$$

where

$$x_n=(2n-1)l$$

is the total distance traveled by the pulse, and where

$$y_n=(2n-1)r\theta k \ .$$

Here α and k are the attenuation coefficient and the wave vector of second sound, respectively.

An experimental echo pattern with a very large number of echoes is shown in Fig. 9. The solid curve is a calculated curve given by Eq. (14) with I_0, α, and θ determined by fitting the intensities of the first seven echoes ($\tau<0.013$ sec) to Eq. (14). The dotted curve corresponds to $\theta=0$.

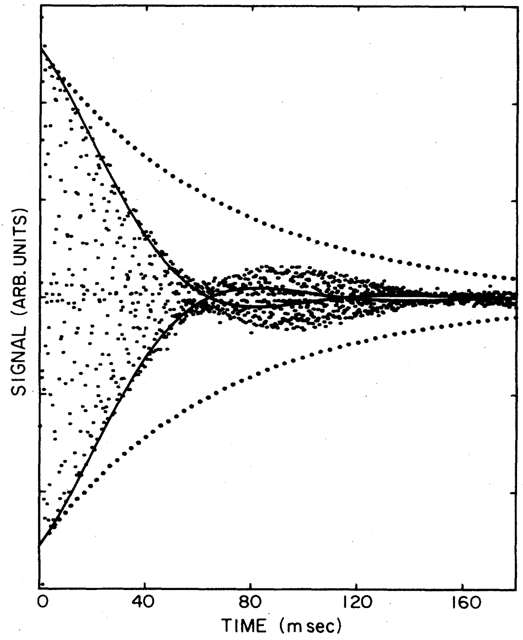

FIG. 9. Pattern obtained from 90 echoes in the medium-length cell at a pressure of about 1 bar and well below T_λ. For this run, $u_2=1228$ cm/sec and $f=40$ kHz. The figure shows about 1200 points taken at intervals of 150 μsec. These points more or less randomly sample some of the cycles in the echoes, and their envelope coincides to a good approximation with the envelope of the echoes. In a separate experiment, the wedge angle θ and the attenuation α were determined from the first seven echoes, corresponding to the initial 0.015 sec in this figure, sampled at 3.3-μsec intervals. The dashed line in the figure is the envelope which corresponds to $\theta=0$ (attenuation only). The solid line corresponds to Eq. (14), which includes attenuation and wedge effects.

For each cell the echo patterns were measured at several frequencies, and the angle θ was determined by fitting the echo intensities to Eq. (14). These measurements were made far away from the λ point where the wedge effects dominated the damping of second sound. Results for θ of the medium-length cell are shown in Fig. 10 as a function of frequency for two different temperatures. They are well represented by a constant average value

$$\theta=(2.91\pm0.13)\times10^{-4} \text{ rad} \ .$$

For the short and the long cells, the measurements gave

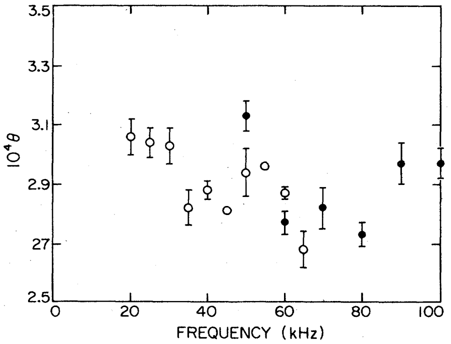

FIG. 10. Plot of the angle between the heater and the bolometer versus second-sound frequency at two different temperatures. The values of θ were obtained by fitting measure echo intensities to Eq. (14). The error bars show the standard error obtained from the fits. Open circles, $u_2=597$ cm/sec; solid circles, $u_2=1051$ cm/sec.

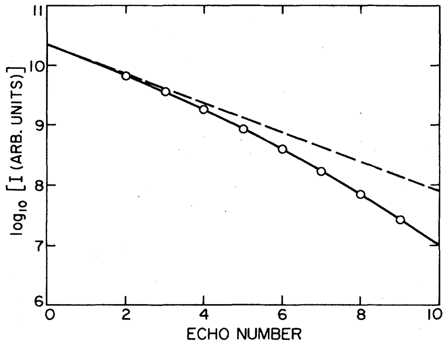

FIG. 11. Typical plot of echo intensities versus echo number. The pressure was $P=14.7$ bars. The solid curve is a fit to Eq. (15), and the dashed curve shows the attenuation in the absence of wedge effects. For this run $u_2=473$ cm/sec, corresponding to $t=4.7\times10^{-3}$ and $f=25$ kHz.

$$\theta=(2.03\pm0.38)\times10^{-4}\text{ rad}$$

and

$$\theta=(1.90\pm0.26)\times10^{-4}\text{ rad},$$

respectively.

Once θ was determined for each cell, it was treated as a fixed parameter. Then, the attenuation coefficient for an echo pattern could be determined by fitting the echo intensities to Eq. (14) with only two adjustable parameters, I_0 and α. In practice, the function used for fitting was

$$\ln(I_n)=\ln(I_0)-2\alpha x_n+\ln\left[\frac{2J_1(y_n)}{y_n}\right]^2 . \tag{15}$$

A typical fit obtained for the medium-length cell is shown in Fig. 11. In this case, both the effects of second-sound damping and the wedge were comparable. The least-squares fit also gave the standard error for the attenuation α.

J. Various sources of attenuation

Aside from the bulk damping, which is of interest to us, there are several other contributions to the attenuation α. We consider them now.

1. *Viscous losses*

When a plane second-sound wave propagates in a cavity, the fluid movement is parallel to the walls of the cavity. Owing to the viscous interaction between the normal fluid and the walls, the second sound is attenuated. The viscous interaction penetrates a characteristic distance $\lambda=(\eta/\rho_n\omega)^{1/2}$ into the liquid from the walls. Here, η and ρ_n are the shear viscosity and mass density of the normal fluid, respectively. The attenuation coefficient α_η is given by[44]

$$\alpha_\eta=\left[\frac{1}{ru_2}\right]\left[\frac{\rho_s}{\rho}\right]\left[\frac{\eta\omega}{2\rho_n}\right]^{1/2}, \tag{16}$$

where ρ_s, ρ_n, and ρ are the superfluid, normal-fluid, and total mass densities, respectively. Thus, viscous losses vanish at T_λ as $\rho_s^{1/2}$. They are quite small in the entire critical region.

2. *Thermal losses*

When second sound is excited in a cavity, thermal gradients are established between the boundaries of the cavity and the liquid helium. The thermal conduction due to the temperature gradients across the boundaries causes an attenuation of second sound. At the walls of a cylindrical cavity, the attenuation is given approximately by[45]

$$\alpha_w=\frac{2}{rCu_2}\frac{\sqrt{f}}{R_w\sqrt{f}+K_w}, \tag{17}$$

where

$$K_w=(\pi C_w\lambda_w)^{-1/2}+(\pi C\lambda)^{-1/2} .$$

Here, C and C_w are the heat capacities per unit volume of liquid helium and the wall material, respectively, λ and λ_w are the thermal conductivities, and R_w is the Kapitza resistance between liquid helium and the walls.

The attenuation due to the ends of the cavity is given approximately by

$$\alpha_e=\frac{1}{lCu_2}\frac{\sqrt{f}}{R_e\sqrt{f}+K_e}, \tag{18}$$

where

$$K_e=(\pi C_e\lambda_e)^{-1/2}+(\rho C\lambda)^{-1/2} .$$

Here, C_e and λ_e are the heat capacity per unit volume and the thermal conductivity of the end material of the cavity, respectively, and R_e is the Kapitza resistance.

In the experiments reported here, the wall material was copper and the end material glass. The bolometer films were very thin compared to the thermal diffusion length. For glass, K_e is so large that α_e is negligible for all frequencies used in the experiments.

For high frequencies, K_w can be neglected and the wall losses become constant at a given temperature. The attenuation is then

$$\alpha_w\simeq\frac{2}{rCu_2R_w} . \tag{19}$$

The Kapitza resistance R_w was determined by measuring the temperature change inside the cavity when the cavity was heated by increasing the power dissipation in the bolometer. The change in temperature was monitored by measuring u_2. The measurements were made close to the λ point where u_2 is very sensitive to small changes in temperature. The Kapitza resistance is given by

$$R_w=A\Delta T/P ,$$

where A is the area of the walls of the cavity, ΔT is the change in temperature, and P is the power dissipation inside the cavity. The measurements gave $R_w\simeq2.2$ cm^2 K/W.

Using copper cells instead of stainless-steel ones was an advantage for two reasons. First, since copper has a much higher thermal conductivity than stainless steel, the power dissipation in the bolometer due to the dc bias did not raise the temperature of the inside of the cavity above that of the surrounding as much as it would have for stainless steel. Second, K_w is much smaller for copper than stainless steel, so that for the second-sound frequencies used in the experiments, α_w [Eq. (19)] was approximately independent of frequency.

3. *End losses*

Two small grooves less than 0.1 mm in diameter and depth, in one cavity end, connected the cavity to the inside of one of the end caps. This facilitated pumping out the cavity and filling it. Since liquid helium could flow through these holes, it could lead to some attenuation of second sound. Experimentally, an attenuation, roughly independent of frequency, was observed in addition to α_w given by Eq. (19). This attenuation, α_0 was approximately 2—3 times larger than α_w. The method of extraction of values of α_0 from the data is explained below.

The attenuation α_0 should be inversely proportional to the length of the cell. The experimental results were consistent with this fact. A good quantitative comparison was, however, not possible because α_0 was small and had rather large statistical errors.

4. *Diffraction losses*

Consider a cylindrical cell with the bolometer not perfectly parallel to the heater but wedged at an angle θ (Fig. 12). The heater produces a circular beam of second sound. The first echo covers the entire area of the bolometer and is reflected at an angle 2θ with respect to the vertical. As a result, if the beam remains collimated, the second echo would cover the area of the bolometer as shown schematically in Fig. 12. On the short-length side of the cell, the second-sound beam shifts a distant $4\theta l$ into the cell. On the long-length side of the cell, part of the beam is reflected back by the walls into the cell. Since the beam is not infinite in its lateral extent, it does not remain a plane wave. It spreads out at an angle λ/a, where λ is the wavelength of second sound. Hence, for low frequencies, when the wavelength is large, the wedge effects would be modified by this diffraction and the modulation of the echo pattern would deviate from the one given by Eqs. (13). In the range of frequencies used for the measurements of second-sound damping, diffraction was a negligible effect.

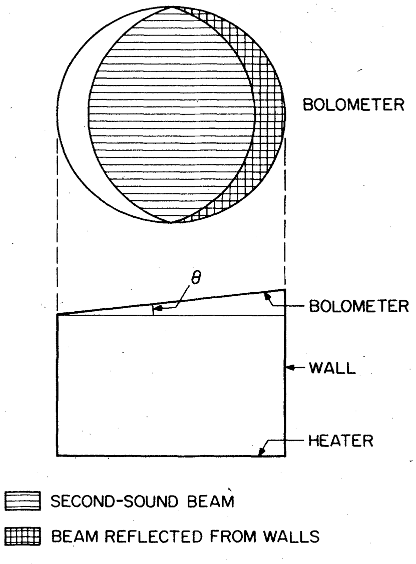

FIG. 12. Schematic diagram to illustrate the effect of diffraction.

K. Finite power and sound amplitude effects

We investigated the effects on the second-sound attenuation due to power dissipation in the bolometer biased by a dc current and due to a finite second-sound amplitude.

Owing to the Joule heating produced at the bolometer by the bias current, a dc counterflow of the normal and superfluid components of liquid helium is set up. This counterflow can affect the attenuation of second sound.[46] The range of power dissipation used for the measurements of damping was approximately 1—7 μW/cm^2. For power dissipation at least a magnitude larger than the ones used for damping measurements, no measurable effect on the second-sound attenuation was observed within the experimental uncertainties. For high-power dissipation, the temperature of the cavity rose above the bath temperature, changing u_2 itself, and then an effect on the attenuation could, of course, be seen. Figure 13 shows the measured values of the attenuation as a function of bolometer-power dissipation at one temperature.

Very significant effects of a finite second-sound amplitude on the attenuation were, however, seen. An empirical study of this effect was made. The attenuation α was measured at a given temperature and frequency as a function of initial second-sound amplitude by the FFT method. Figure 14 shows a plot of the attenuation α as a function of the square of the second-sound amplitude for two reduced temperatures. The curves were fitted with the empirical function

$$\alpha = a + bA^2 , \tag{20}$$

where A is the amplitude of second sound. Figure 15 is a log-log plot of the slope b as a function of reduced temperature (the slope b was also weakly dependent upon the frequency). For measurement of the damping, the amplitude of second sound was always kept sufficiently low so that its effect on the attenuation α was no more than 2—3 %.

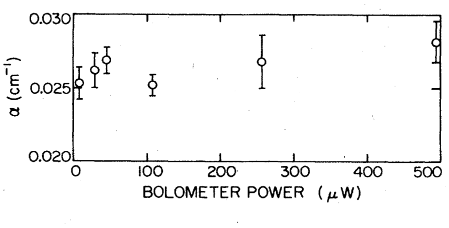

FIG. 13. Plot of α versus the power dissipation in the bolometer in the medium-length cell at vapor pressure, $t = 10^{-3}$ ($u_2 = 318$ cm/sec), and $f = 10$ kHz.

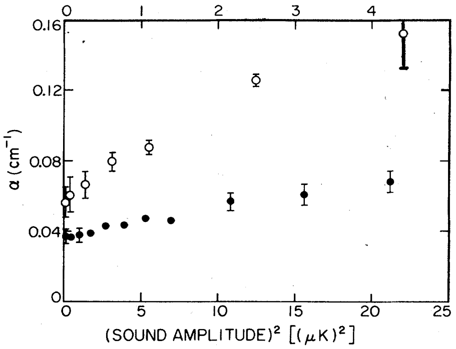

FIG. 14. Plot of α versus the square of the second-sound amplitude generated by the heater at two different temperatures for the medium-length cell. Open circles: $t=4.05\times10^{-4}$ and $f=9$ kHz (upper scale). Solid circles: $t=2.13\times10^{-3}$ and $f=20$ kHz (lower scale).

L. Extraction of the damping coefficient D_2 from data

The total attenuation α can be written as

$$\alpha=\alpha_2+\alpha_\eta+\alpha_w+\alpha_e+\alpha_0+\alpha_d\ , \tag{21}$$

where α_2 is the bulk attenuation which is of interest to us, α_0 is the attenuation due to end losses discussed in subsection J 4 above, and α_d is the attenuation due to diffraction. As discussed above, α_e is negligible. At high frequencies, α_d can be neglected and α_w becomes a constant [Eq. (19)]. The viscous attenuation α_η can be calculated from Eq. (16). Hence, at high frequencies,

$$\alpha-\alpha_\eta\simeq\alpha_2+\widetilde{C}\ , \tag{22}$$

where $\widetilde{C}$ is a constant given by

$$\widetilde{C}=\alpha_0+\frac{2}{rCu_2R_w}\ . \tag{23}$$

The attenuation α_2 is related to the frequency-independent damping coefficient D_2 by

$$\alpha_2=\frac{1}{2}\frac{\omega^2}{u_2^3}D_2\ . \tag{24}$$

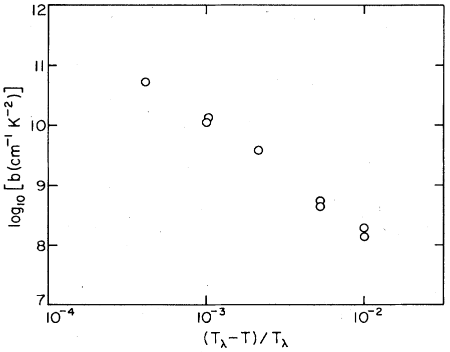

FIG. 15. Double-logarithmic plot of the slope of α versus sound intensity curves against the reduced temperature. Two points at some reduced temperatures correspond to different second-sound frequencies in the ratio 2:3 approximately. The slope b is slightly smaller at lower frequencies.

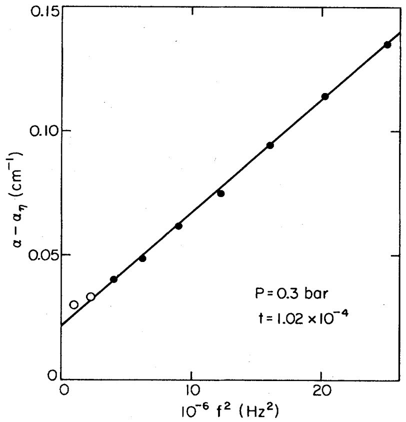

FIG. 16. Typical plot of $\alpha-\alpha_\eta$ versus f^2 obtained in the medium-length cell at 0.3 bar. The solid circles are fitted to a straight line whose slope determines $D_2=5.33\times10^{-4}$ cm^2/sec.

From Eqs. (22) and (24) it can be seen that a plot of $\alpha-\alpha_\eta$ versus the square of the frequency should be linear at high frequencies. The slope determines D_2 and the intercept gives the constant $\widetilde{C}$.

A typical plot of $\alpha-\alpha_\eta$ versus the square of the frequency for the medium-length cell is shown in Fig. 16. The solid line is a least-squares fit to the high-frequency points plotted as solid circles. The standard error for the slope of the linear fit was also obtained from the least-squares analysis. This determined the standard error for D_2. A similar plot for data taken in the long cell at the much larger reduced temperature 0.1 already was shown elsewhere.[32]

The intercept in Fig. 16, and in Fig. 1 of Ref. 32, is larger than the estimate α_w given by Eq. (19) and shows the existence of α_0. The open circles at low frequencies, particularly in Fig. 1 of Ref. 32, show the presence of diffraction effects. Since the thermal losses vanish at zero frequency [Eq. (17)], the experimental points would lie below the linear fit if diffraction effects were absent.

III. RESULTS

Measurements of the second-sound velocity and attenuation resulted in the values of D_2 and u_2 listed in Table I. Each of the 54 values of D_2 is based typically on attenuation measurements at 10 different frequencies. Each attenuation measurement at a given frequency is based typically on the analysis of 5 to 10 echoes and Eq. (15). Corrections for viscous losses α_η [Eq. (16)] were applied, and α_2/f^2 was obtained from a least-squares fit of $\alpha-\alpha_\eta$ to a linear function of f^2 (see Sec. II L). D_2 was derived from α_2/f^2 using Eq. (24). The analysis also yielded the random errors of D_2 listed in the table. Additional systematic errors primarily due to uncertainties in the wedge angle θ (see Sec. II I) are perhaps 1% or 2%. These systematic errors will influence all data taken in the same cell in a similar way.

The measurements were made primarily in the cell of medium length. In order to test for systematic errors associated with reflection losses, some measurements were also performed in the short and long cells (see footnotes to

TABLE I. Experimental measurements of the second-sound velocity u_2 and the second-sound damping D_2. The reduced temperature t is derived from u_2 and Ref. 41. Except as noted, the measurements were made in the cell of length 1.225 cm.

10^3t	u_2 (cm/sec)	10^4D_2 (cm^2/sec)
	Vapor pressure	
164[a]	1978	10.7 ± 0.2
100[a]	1761	5.58 ± 0.11
60.3[a]	1519	4.01 ± 0.20
36.5[a]	1287	3.51 ± 0.13
21.5[a]	1050	3.28 ± 0.02
21.5	1050	3.10 ± 0.07
10.0[a]	781	3.11 ± 0.07
4.98	598	2.98 ± 0.05
5.00[a]	598	3.08 ± 0.02
2.15	328	3.20 ± 0.07
1.00	317	3.43 ± 0.13
0.405	226	3.77 ± 0.07
0.405[b]	226	3.87 ± 0.12
0.208[b]	172	4.35 ± 0.19
0.120[b]	141	5.08 ± 0.16
	$P=0.3$ bar	
0.102	132	5.33 ± 0.05
0.0685	113.8	5.53 ± 0.09
0.0465	98.5	6.26 ± 0.12
0.0342	87.9	7.15 ± 0.15
0.0224	75.2	7.72 ± 0.29
	$P=6.9$ bars	
20.4	957	3.57 ± 0.11
9.7	706	3.34 ± 0.13
4.62	524	3.27 ± 0.04
	$P=14.7$ bars	
65	1305	5.07 ± 0.09
25.0	939	4.17 ± 0.09
10.0	650	3.69 ± 0.09
	$P=14.7$ bars	
4.66	473	3.54 ± 0.10
2.07	341.4	3.44 ± 0.08
1.00	255.7	3.48 ± 0.06
0.432	184.3	3.64 ± 0.09
0.231	144.5	3.90 ± 0.06
0.1008	105.3	4.06 ± 0.03
0.0647	89.0	4.39 ± 0.11
0.0362	71.5	4.94 ± 0.19
	$P=22.3$ bars	
46.8	1080	5.14 ± 0.08
21.2	798	4.38 ± 0.08
10.0	582	4.06 ± 0.05
4.59	422	3.85 ± 0.05
2.16	310	3.66 ± 0.02
1.00	228	3.67 ± 0.09
0.481	170.4	3.75 ± 0.06
0.216	124.5	3.76 ± 0.07
0.096	90.8	4.13 ± 0.05
0.059	75.3	4.25 ± 0.10
	$P=28.0$ bars	
45.7	1007	5.73 ± 0.09
21.7	742	4.94 ± 0.07
9.88	532	4.42 ± 0.08
4.53	384	3.99 ± 0.05
2.09	279	3.66 ± 0.03
1.00	206.8	3.54 ± 0.05
0.471	152.6	3.67 ± 0.10
0.214	111.5	3.54 ± 0.07
0.098	82.1	3.88 ± 0.13
0.050	63.5	3.87 ± 0.18

[a] Cell length 3.678 cm.

[b] Cell length 0.404 cm.

Table I). These results for D_2 do not differ systematically from the ones obtained in the medium-length cell.

The second-sound—velocity values listed in Table I were derived from the time of flight of our second-sound pulses with an accuracy of typically 0.2%. The reduced temperatures were in most cases obtained from u_2 and the measurements of Greywall and Ahlers.[41] Only some values of t rather far away from T_λ are the result of new direct temperature measurements.

The measurements at vapor pressure (VP) could be performed only for $t \gtrsim 10^{-4}$ because the bath temperature could not be regulated well for temperatures closer to T_λ. We thus made some measurements at 0.3 bar. At that pressure, the sample $T_\lambda(P)$ was reduced below the bath value of T_λ by about 3 mK, and measurements closer to $T_\lambda(P)$ were thus possible. At constant

$$t=[T_\lambda(P)-T]/T_\lambda(P) ,$$

the value of D_2 is not very sensitive to changes in P. The increase in D_2 due to a change in P from VP to 0.3 bar for constant $t \lesssim 10^{-4}$ is only about 0.4%. Thus, the 0.3-bar data are directly comparable with the VP data.

Results were obtained primarily at VP, 14.7, 22.3, and 28.0 bars. The first three pressures were chosen because thermal-conductivity data exist at those pressures,[13] making a direct comparison with the theory possible without the need for interpolation of the data. The 28-bars data complete the measurements over the entire pressure range of the transition. A few measurements were made also at 6.9 bars, but only at relatively large values of t, because only there was the pressure dependence of D_2 sufficiently large to warrant the additional effort of taking more data.

The smallest value of t at which measurements were obtained was determined by the rapid increase, approximately proportional to $t^{-1.45}$, of α_2 as T_λ is approached. The attenuation had to be sufficiently small to permit the observation of several echoes in order to determine α_2 reliably by our method. Since $\alpha_2 \propto f^2$, the increase in α_2 with decreasing t can, in part, be compensated for by a shift of the frequency range used in the experiment. However, the smallest frequency must satisfy $f \gg u_2/l$ so that a tone burst of several cycles will fit into the cell of length l.

For the above reasons the range of data is limited to $t \gtrsim 2\times10^{-5}$ at VP. At the highest pressure, measurements were not possible by our technique for $t \lesssim 5\times10^{-5}$. Even though D_2 decreases with increasing P at small constant t, $\alpha_2 \propto D_2/u_2^3$ increases considerably, thus restricting the experimental range to larger values of t at higher P.

In Fig. 17 we compare our results at VP and 0.3 bar (solid circles) with previous measurements at VP. We will take the opportunity in Fig. 20 below to display our VP and 0.3-bar data by different symbols. For our data we show error bars corresponding to random errors whenever these extend beyond the solid circles. The results of Crooks and Robinson[30] are shown as open circles, and those of Ahlers[29] as open triangles. Only a few representative error bars are included with these data in order to avoid crowding the figure. The agreement between our new data and the older results for $t \lesssim 10^{-3}$ is much better than could have been expected on the grounds of the error estimates. For $t \gtrsim 10^{-2}$ our results are systematically lower than those of Crooks and Robinson, but only by about their estimate of their possible systematic errors. In the region $t \approx 0.1$, where α_2 is quite small and thus difficult to measure, our data agree well with those of Hanson and Pellam (HP).[28] For $t \lesssim 0.1$ the difference between our results and HP's can be attributed to considerable systematic errors in the HP data for D_2 associated with temperature-scale uncertainties. Hanson and Pellam[28] unfortunately did not report values of u_2, and quote only α_2/ω^2 and T. Although $u_2(T)$ is well known,[41] the uncertainty in T leads to rather large uncertainties in u_2 in the region near T_λ where u_2 varies rapidly, thus introducing appreciable systematic errors into D_2 (which is proportional to u_2^{-3}). We conclude that there is complete consistency between all the data shown in Fig. 17 (see, however, Ref. 31).

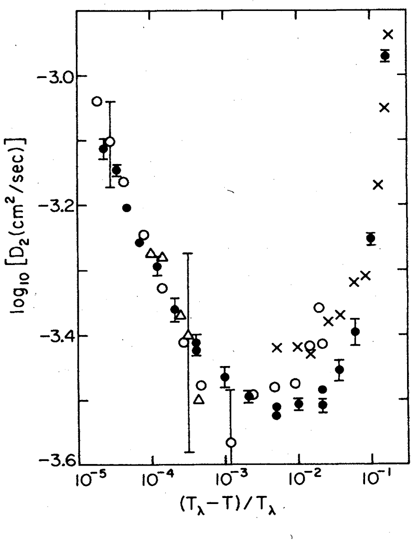

FIG. 17. Experimental results for the second-sound damping D_2 at vapor pressure as a function of the reduced temperature $t=1-T/T_\lambda$ on logarithmic scales. Open circles, Ref. 30; open triangles, Ref. 29; crosses, Ref. 28; solid circles, this work. For the data of Refs. 29 and 30 only a small number of representative error bars are shown to avoid crowding the figure. For the present work, error bars are shown whenever they extend beyond the size of the solid circles.

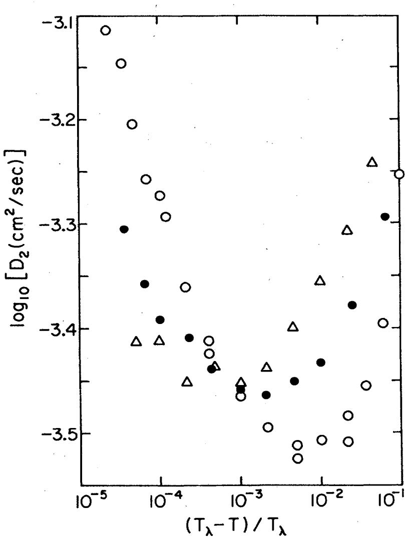

FIG. 18. Experimental results for the second-sound damping D_2 at three different pressures as a function of the reduced temperature $t=1-T/T_\lambda(P)$ on logarithmic scales. Open circles, vapor pressure and 0.3 bar; solid circles, 14.7 bars; open triangles, 28.0 bars. The data illustrate the intricate pressure dependence of D_2 at constant t which changes sign near $t=8\times10^{-4}$.

In Fig. 18 we show our results at VP, 14.7 bars, and 28.0 bars as a function of t on logarithmic scales. This figure illustrates the dramatic change in the pressure dependence of D_2 as T_λ is approached. The measurements at all pressures cross at a very nearly unique reduced temperature of about 8×10^{-4}. The data illustrate that the critical region, in which the divergence of D_2 at T_λ becomes noticeable, is very narrow at all P and becomes narrower as P increases. The same phenomenon was observed in the pressure dependence of the thermal conductivity above T_λ.[13]

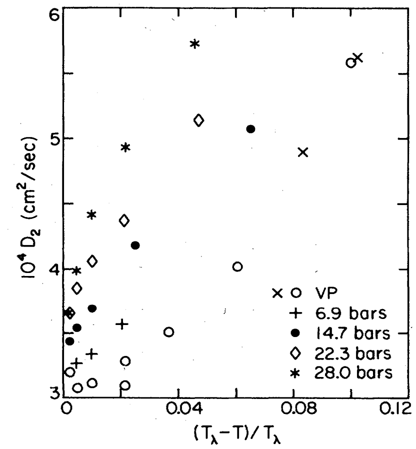

FIG. 19. Experimental results for the second-sound damping D_2 as a function of $t=1-T/T_\lambda$ on linear scales. Data in the critical region, which is only very close to the left edge of the figure, are omitted. Crosses, Ref. 28. All other data are from the present work.

Figure 18 already shows that D_2 also increases rather dramatically at large t, well away from T_λ. This region is displayed more appropriately on linear scales as in Fig. 19. Here, data in the critical region, which is in the immediate vicinity of the left ordinate, are omitted. At all pressures, D_2 is seen to be a very strong function of T. At VP, for instance, it increases by about 35% when the temperature is decreased by 4% from 2.04 K ($t \simeq 0.06$) to 1.96 K ($t = 0.10$).

IV. COMPARISON WITH THEORY

As discussed in the Introduction, the analysis of the thermal conductivity above T_λ (Refs. 25 and 26) in terms of the recursion relations[18,19] for model F fixes the nonuniversal parameters in the theory by providing initial values for the integration of these relations. That integration then yields the dynamic parameters f and w which are related to the order-parameter and entropy relaxation rates. Having obtained f and w from the analysis *above* T_λ, it is possible, in principle, to predict the second-sound damping *below* T_λ without any further adjustable parameters.[24] In practice, there are a number of potential problems. First, we mention the uncertainty in the experimental input above T_λ. There, the existing measurements of the thermal conductivity depend surprisingly strongly on the spacing d between the plates of the conductivity cell, even for d much larger than the correlation length ξ.[11] This effect is difficult to understand theoretically, but in any event the renormalization-group-theory predictions in their present form pertain to the infinite-size (bulk) limit. Measurements in a cell of reasonably large d (cell A) are available only at vapor pressure.[25] Since we would like to compare the pressure dependence predicted by the theory with the D_2 data, we are forced to make the comparison on the basis of thermal-conductivity data obtained in a somewhat narrower gap (cell D),[13] which may not quite correspond to the bulk limit. Therefore, we first examine in Fig. 20 the difference in the predicted values[25] of D_2 at VP based on the two cells, and look upon it as an estimate of the uncertainty in the prediction due to uncertainties in the nonuniversal parameters of the theory. The solid line and the short-dashed line are based on the model-F analysis by Ahlers, Hohenberg, and Kornblit (AHK) of the cell-A and -D thermal-conductivity data, respectively, using the formula by Dohm and Folk[24,27] which gives the dependence of D_2 upon f and w for model E. The cell-A-based prediction agrees reasonably well with the data for $t \lesssim 10^{-3}$, but fails to agree by as much as 25% for larger t. At small t the cell-D-based prediction is slightly worse than the cell-A-based result.

The disagreement displayed in Fig. 20 between theory and experiment is largest near $t \simeq 10^{-2}$. In a sense, this is surprising because it is in this temperature range that the dynamic coupling constant f is a small parameter and that the perturbation expansion of the theory should be valid.[25] There are, however, a number of approximations involved in applying the theory to this problem. First, the recursion relations used[25] for fitting the conductivity λ were truncated at second order in f, with only the first-order term based on model F and the second-order term taken from model E. The relationship $\lambda(f,w)$ that was used was truncated after the first-order term. A recent analysis[26] of the cell-A data based on an as yet unpublished model-F expansion to second order in f [but retaining the first-order expansion of $\lambda(w,f)$] has yielded values of D_2 very similar to the cell-A-based data shown in Fig. 20, suggesting that the approximations in the recursion relations may be unimportant in the experimental temperature range.

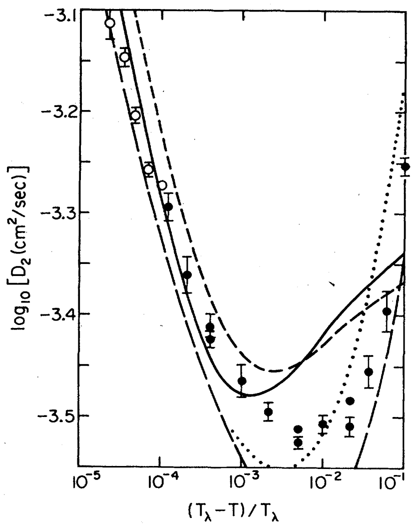

FIG. 20. Comparison of the second-sound damping D_2 at vapor pressure with theoretical predictions. Solid circles, data at vapor pressure; open circles, data at 0.3 bar. The change in D_2 with pressure at constant t between VP and 0.3 bar is negligible. Solid line, prediction from Ref. 25 based on cell-A thermal-conductivity measurements; short-dashed line, prediction from Ref. 25 based on cell-D thermal-conductivity measurements; long-dashed line, prediction from Ref. 33; dotted line, prediction from Ref. 34 (however, see Ref. 36 for a critique of this theory).

Searching further for possible reasons for the disagreement shown in Fig. 20, we note that the theory below T_λ involves *static* parameters which do not enter the relations above T_λ.[24,27] They are the ratio of the longitudinal to the transverse correlation length, $\xi^{\mathrm{L}}/\xi^{\mathrm{T}}$, and the static coupling constant u. The ratio $\xi^{\mathrm{L}}/\xi^{\mathrm{T}}$ is universal and can, in principle, be calculated from the theory of the static properties. In practice, the value of $\xi^{\mathrm{L}}/\xi^{\mathrm{T}}$ has not yet been obtained with high numerical accuracy. The static coupling constant u is not universal, but its value has been estimated in a number of ways. In Fig. 20 we used the second-order ϵ-expansion fixed-point value $u^* = 0.04$. The possibly more accurate fixed-point value $u^* = 0.0363$ was obtained recently[47] from a high-order ϵ-expansion calculation at $d = 3$.[48] Since u^* is not universal, there seems to be no *a priori* reason to assume it to be pressure independent. However, evidence against an appreciable pressure dependence comes from a recent prediction by Dohm[47] which relates u^* to the experimentally accessible specific heat C_p. A one-loop calculation[47] can be used[49] to show that, *to this order* in perturbation theory and for the renormalization procedure used by Dohm, u^* depends only on the universal specific-heat—amplitude ratio A/A', and on the universal exponents α and ν. This calculation and experimental data yield the value $u^*=0.0343$, independent of pressure[49] and in good agreement with the ϵ-expansion result for $d=3$.[48] We conclude that, at present, we are at liberty to make some adjustments in ξ^L/ξ^T and possibly minor changes in u^*, but that the values used should be the same at all pressures. It turns out that adjusting either u or ξ^L/ξ^T by a multiplicative factor has nearly the same effect on the theory of displacing the curves in Fig. 20 vertically.[25] Therefore, the uncertainty in the static parameters permits, in practice, only a single significant adjustment which has little influence on the shape of the predicted curves. We chose to change ξ^L/ξ^T from 0.33 to 0.28 (changing u from its second-order ϵ-expansion fixed-point value $u^*=0.040$ used in Fig. 20 and Ref. 25 to $u=0.030$ has a very similar effect). This resulted in agreement between theory and experiment at vapor pressure and $t=$ 0.005 where the cell-A- and cell-D-based predictions are the same. The cell-D-based result is shown as a solid line in Fig. 21(a). The dashed line is the unadjusted prediction. The solid curve agrees well with the data for small t also, but in the intermediate range near $t\approx 10^{-3}$ the theory differs from the data even after the adjustment. For the cell-A-based prediction, the disagreement at $t<0.005$ is larger than for the cell-D result. Thus we conclude that a multiplicative adjustment, independent of t, in the static parameters, does not yield a quantitative fit of the theory to the data.

At elevated pressures, conductivity data exist only for cell D. Thus, we show the cell-D-based predictions at 14.7 and 22.3 bars in Figs. 21(b) and 21(c) together with the experimental data. As in Fig. 21(a), the dashed lines correspond to $\xi^L/\xi^T=0.33$ and the solid lines to $\xi^L/\xi^T=0.28$. As we saw at VP, it is apparent also at elevated P that the data have a t dependence which differs somewhat from the theory, but the effect of pressure on the damping is predicted rather well. Thus, near $t=0.005$, D_2 increases by about 30% in both theory and experiment as P changes from 0 to 22.3 bars. At small t both the experimental and theoretical D_2 decrease considerably with increasing P. Thus the intricate pressure dependence of the measurements which was illustrated in Fig. 18 is largely contained in the prediction.

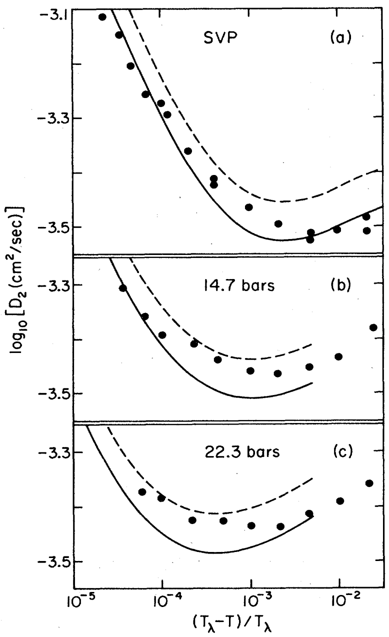

FIG. 21. Second-sound damping D_2 at three different pressures. The data points are the present measurements. The dashed lines are predictions from Ref. 25 based on cell-D thermal-conductivity measurements. The solid lines are the corresponding predictions obtained by changing the correlation-length ratio ξ^L/ξ^T from 0.33 to 0.28. The data illustrate that the pressure dependence of D_2 is given quite well by the theory. The temperature dependence of the data differs in detail from the theory systematically at all pressures.

Very recently, it was emphasized by Dohm[47] that the temperature dependence of the renormalized coupling constant $u(t)$ could be taken into consideration in the calculation of D_2. Dohm's one-loop calculation of the relation between $u(t)$ and C_p, together with experimental data for C_p derived from thermal-expansion—coefficient measurements,[42,49] yields $u^*=0.0343$ and a significant dependence of u upon t particularly at the higher pressure.[47–49] As an illustration of the effect that can be expected from including the temperature dependence of $u(t)$ in the theory, we retained $\xi^L/\xi^T=0.33$ and used $u(t)$ based on an analysis with a specific-heat exponent $\alpha=-0.016$ (see Eqs. 2.15b, 3.16, 3.18, and 3.19, and Tables 4 and 6, of Ref. 49) instead of u^* to calculate D_2. The results are compared, in Fig. 22, with the experimental data. The solid lines are based upon $u(t)$, whereas the short-dashed lines correspond to $u=u^*=0.0343$. The

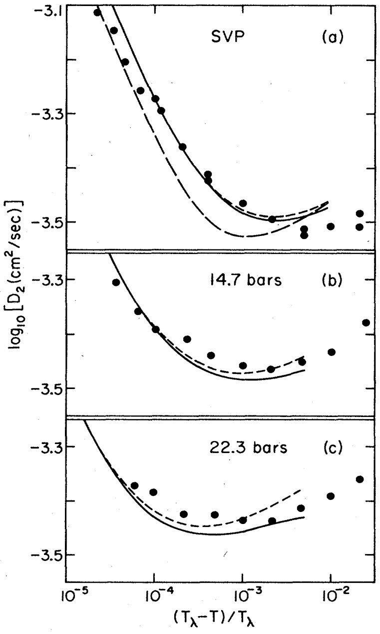

FIG. 22. Second-sound damping at three different pressures. The solid lines are predictions based on cell-D thermal-conductivity measurements and a temperature-dependent static coupling constant $u(t)$ (Refs. 47 and 49). The short-dashed lines correspond to $u=u^*=0.0346$. The long-dashed line in (a) is based on cell-A thermal-conductivity measurements and $u(t)$.

temperature dependence of $u(t)$ clearly has a significant influence on the predicted D_2, particularly at the higher pressures. Nonetheless, this use of $u(t)$ directly in the existing formula[27] for D_2 does not yield perfect agreement. In Fig. 22(a) we show the prediction based on $u(t)$ and cell A as a long-dashed line. It does not agree as well with the data as the cell-D-based result.

Most importantly, it appears to us that a likely reason for the disagreement between theory and the data displayed in Figs. 20—22 may be the use of model E for calculating the relation $D_2(w,f)$. As discussed in the Introduction, this model does not treat properly the coupling of the specific heat to the order parameter. Even if the specific heat is taken into account *ex post facto* within model E, resulting in the correct asymptotic behavior (model E_S of AHK), the dynamics at finite t differs significantly from that of model F, and, for example, gives values for λ considerably too large for t near 10^{-2} (Fig. 8 of Ref. 25). Although in the case of the D_2 prediction the recursion relations are based on model F and only the relation $D_2(w,f)$ is derived from model E_S, we consider this approximation in the theory the most likely source of the disagreement with the data.

In Fig. 20 we also compare the new measurements at vapor pressure and 0.3 bar with the theory of Ferrell and Bhattacharjee. The long-dashed line corresponds to their original prediction.[33] In the range $t \gtrsim 10^{-3}$, their prediction falls considerably below the data with a maximum difference of about 20% near $t \approx 10^{-2}$. More recently, these authors claimed that they had originally omitted a contribution to D_2 and presented a correction to their prediction[34] which yields the dotted line in Fig. 20. However, the validity of their estimate of the size of that correction has been questioned recently,[36] and therefore the comparison of the data with the dotted curve should be treated with caution. To our knowledge, the theory of Ferrell and Bhattacharjee has not yet been applied at higher pressures.

V. COMPARISON WITH FIRST-SOUND DAMPING

It is interesting to compare D_2 with the first-sound damping D_1 by means of the hydrodynamic equations which give the damping in terms of the thermal conductivity and the viscosities. We have[50]

$$D_2=(\rho_s/\rho_n\rho)(\tfrac{4}{3}\eta+\zeta_2+\rho^2\zeta_3-2\rho\zeta_1)+\lambda'/C_p \qquad (25)$$

and

$$D_1=\rho^{-1}(\tfrac{4}{3}\eta+\zeta_2)\,. \qquad (26)$$

From the measurements above T_λ,[12,13] one may estimate[33,34,36] that the singular contribution to λ'/C_p in Eq. (25) is quite small for $t \gtrsim 10^{-3}$. Therefore, in the region not too far from T_λ, but for $t \gtrsim 10^{-3}$, the contribution λ'/C_p to D_2 can be obtained roughly from an extrapolation of the background conductivity $\lambda_\infty(T)$ above T_λ (fit 4 of Table VIII of Ref. 25) to the range $T<T_\lambda$, and from the experimental specific heat[51] below T_λ. In Fig. 23 we show D_2 (solid circles), and $D_2-\lambda_\infty/C_p$ as an estimate of $D_2-\lambda'/C_p$ (open circles), at VP.

We wish to compare $D_2-\lambda'/C_p$ with $(\rho_s/\rho_n)D_1$ since these two quantities differ only by the term involving $\rho^2\zeta_3-2\rho\zeta_1$. Although there have been many investigations of first-sound damping, most of them have concentrated on the region very near T_λ, and many have discarded any "background" damping (which would be noticeable only further away from T_λ) together with various extraneous contributions.[52] The only measurements we are aware of in the temperature range of interest here, of the full bulk attenuation at hydrodynamic frequencies, are those by Chase.[53] In Fig. 23 we show as solid squares the values of $(\rho_s/\rho_n)D_1$ corresponding to Figs. 3 and 6 of Ref. 53. It is apparent that the difference between these data and $D_2-\lambda'/C_p$, which corresponds to $(\rho_s/\rho_n\rho)(\rho^2\zeta_3-2\rho\zeta_1)$, is nearly independent of t for $10^{-3} \lesssim t \lesssim 10^{-1}$ and about equal to 1.0×10^{-4} cm²/sec.[54]

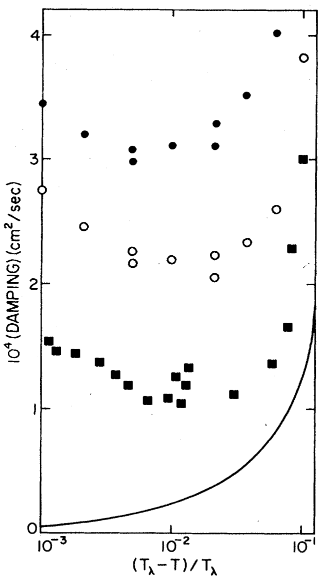

FIG. 23. Comparison of various contributions to first- and second-sound damping D_1 and D_2. Solid circles, D_2; open circles, $D_2-\lambda'/C_p$ (λ' is the thermal conductivity and C_p the specific heat); solid squares, $(\rho_s/\rho_n)D_1$; solid line, $\frac{4}{3}(\rho_s/\rho_n\rho)\eta$, where η is the shear viscosity.

For comparison, we show in Fig. 23 as a solid line the contribution $\frac{4}{3}(\rho_s/\rho_n\rho)\eta$ from the shear viscosity[55] to D_2. This contribution vanishes at T_λ as ρ_s/ρ_n, since η remains finite. It is relatively small for $t \lesssim 10^{-2}$.

Since $(\rho_s/\rho_n)D_1$ is nearly constant for $10^{-3} \lesssim t \lesssim 10^{-1}$, it follows that D_1 itself has the temperature dependence of ρ_n/ρ_s and thus depends strongly upon t over this range. Therefore, the full width of the *static* critical region $t \lesssim 10^{-1}$ manifests itself in D_1 (and thus, of course, also in ζ_2), whereas D_2 shows a strong rise only in the much narrower *dynamic* critical region $t \lesssim 10^{-3}$. This is illustrated in Fig. 24, where, for example, D_1 increases by a factor of 9 from about 2.5×10^{-4} to about 22×10^{-4} cm²/sec over the narrow range of T corresponding to $0.003 \lesssim t \lesssim 0.05$. Over the same range, D_2 and $(\rho_s/\rho_n)D_1$ are nearly constant. It is evident from Fig. 24 that an approximate "background" value can be assigned to $(\rho_s/\rho_n)D_1$,[36] but not to D_1 itself as attempted by Ferrell and Bhattacharjee.[34]

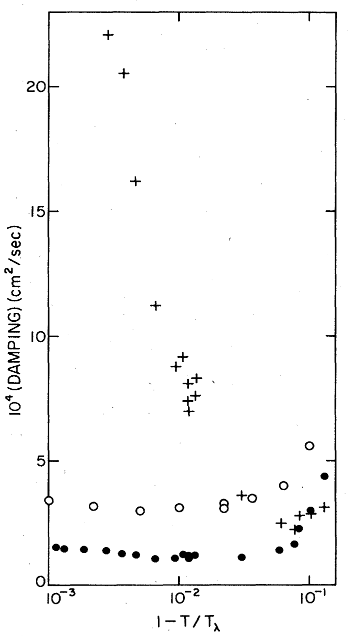

FIG. 24. Comparison of first-sound damping D_1 and second-sound damping D_2. Solid circles, $(\rho_s/\rho_n)D_1$; open circles, D_2; crosses, D_1.

For $t \gtrsim 10^{-1}$ both D_2 and $(\rho_s/\rho_n)D_1$ are strongly dependent upon T because of quasiparticle scattering processes whose temperature dependence is unrelated to the phase transition.[56] For D_2 this strong dependence upon T was mentioned already in connection with Fig. 19.

VI. DISCUSSION AND SUMMARY

In this paper we presented measurements of second-sound damping which have an accuracy of 2–4%. The accuracy achieved in this work is an improvement by nearly an order of magnitude over the best previous data.[30] The results cover the pressure range from vapor pressure to near the freezing line (≈ 28 bars), whereas previous work[28–30] was confined entirely to vapor pressure. At each pressure, the temperature range of the data is roughly from 50 or 100 μK below $T_\lambda(P)$ to 0.1 or 0.2 K below $T_\lambda(P)$.

The experimental procedure used in this work is described in detail. The measurements are based on a tone-burst method which included the following features:

(1) Superconducting bolometers with a temperature resolution of 10^{-8} were developed.

(2) Signal-averaging techniques which enhanced the above resolution by an order of magnitude were used.

(3) Spectral-analysis techniques which eliminated the influence of higher harmonics on echo intensities were employed when appropriate.

(4) A novel half-wave rectification method was developed which virtually eliminated the detrimental effect of temperature noise on signal averaging.

(5) Quantitative corrections were applied for the effect of nonparallelism of the cell ends.

(6) Viscous wall losses were calculated from hydrodynamics and were subtracted.

(7) The effect of thermal wall- and end-losses was considered and eliminated in the data analysis.

(8) Diffraction losses were shown to be negligible.

(9) A careful study was made of finite bolometer-power and sound-amplitude effects, and it was demonstrated that all the present measurements were made essentially in the zero-power and zero-amplitude limits.

A distinct advantage of the tone-burst method is that it permits the use of rather high frequencies. Resonance methods, which have been used in much of the previous work,[29–31] are confined to small frequencies and are therefore influenced more strongly by extraneous damping mechanisms (wall losses, etc.).

The overall features of our results are most evident from Fig. 18. Looking first at the data at vapor pressure (open circles), it is apparent that the critical region, in which the damping manifests its divergence by rising obviously above its background value, is confined to the range $t \lesssim 10^{-3}$. Above T_λ, a narrow critical region had been observed already in the thermal-conductivity measurements.[11–13] There it has been explained[25] in terms of an anomalously small, bare dynamic coupling constant for liquid helium. Below T_λ, the dissipative coupling u from the fourth-order term in the free energy also contributes to the critical dynamics, and thus there is no *a priori* reason for the critical region to be more narrow than it is for static properties.[35] However, the data show that this effect is weak, and that, effectively, the dynamic critical region is also anomalously narrow below T_λ. The data in Fig. 18 show that the critical region becomes even narrower, by more than a decade, as the pressure increases to 28 bars (open triangles). This reduction in width is also observed above T_λ,[13] and there it can be attributed to a further depression of the bare dynamic coupling constant with increasing pressure which results from the combined effects of a decrease in T_λ, a decrease in the entropy at T_λ, and an increase in the background conductivity with increasing pressure [see the discussion in Sec. IV B 1 of AHK (Ref. 25)]. At a given pressure, the width of the critical region below T_λ is more narrow by about a factor of 2 than it is above T_λ.

The narrow critical region of the dynamics is in clear contrast to the behavior of the static properties which start to diverge already for, say, $t \lesssim 10^{-1}$. Because of the wide static critical region, the range $10^{-3} \lesssim t \lesssim 10^{-1}$ should not simply be regarded as a "background" region, for, in a systematic treatment of the dynamics (as can be provided by model F and the renormalization-group theory), the static properties are coupled to the dynamic variables and influence the detailed size of the transport properties. Above T_λ, this coupling is through the specific heat, and its effect is illustrated, for instance, in Fig. 8 of AHK.[25] Below T_λ, this precritical coupling exists even within model E (which neglects the specific heat) because of the dissipative coupling from the coefficient u of the fourth-order term in the free energy. Thus, it is not possible to extract quantitative estimates of the "background" values of the various diffusivities by simply looking in this region, as has been done by Ferrell and Bhattacharjee[20,33,34] using a model which neglects the dissipative coupling [meaningful definitions can be given for such background values in terms of extrapolations to $t=\infty$ of the dynamic variables f and w, as was done by AHK (Ref. 25)]. Contrary to a recent statement by Ferrell and Bhattacharjee,[34] renormalization effects do take place in the range $10^{-3} \lesssim t \lesssim 10^{-1}$, albeit on a somewhat more subtle level, due to the coupling of the dynamic variables to the statics.

Returning to the data in Fig. 18, we note that the damping appears to increase also rather dramatically with *increasing* t in the decade $10^{-2} \lesssim t \lesssim 10^{-1}$. This effect is shown on linear scales in Fig. 19 and has its origin in the strong temperature dependence of quasiparticle scattering processes below T_λ.[56] It should not be considered as being associated particularly with the phase transition (i.e., as a function of t), but rather it should be regarded as an exceptionally strong dependence upon the absolute temperature T.

The results of our measurements have been compared in considerable detail with the various predictions which have been made on the basis of theory and the measured thermal conductivity above T_λ. The comparison provided in Fig. 20 shows that the *qualitative* features of the t dependence of the data are reproduced by the predictions, but the *detailed* temperature dependence is not given correctly at the level of the experimental accuracy. The comparison with the renormalization-group-theory prediction suffers considerably from the ambiguity in the thermal-conductivity measurements above T_λ, and an important future project will consist of resolving this experimental issue; however, the level of disagreement between prediction and data is greater than the ambiguity due to the experimental uncertainty above T_λ. Clearly, one would like to have a more complete calculation of D_2 and λ carried out consistently to, say, two-loop order and based entirely upon model F both above and below T_λ. On the other hand, it is gratifying that the intricate pressure dependence of the data (which is illustrated in Fig. 18) is reproduced rather well already by the theory in its present form. This is illustrated in Fig. 21.

ACKNOWLEDGMENTS

We are grateful for stimulating discussion with P. C. Hohenberg regarding the comparison of our measurements with theoretical predictions. This work was supported by the National Science Foundation under Grant No. DMR-79-23289.

---

*Present address: Division of Electrical and Electronic Standards, National Physical Laboratory, Hillside Road, New Delhi 110012, India.

[1] G. Ahlers, Rev. Mod. Phys. **52**, 489 (1980).

[2] G. Ahlers, in *Phase Transitions*, edited by M. Levy, J. C. Le Guillou, and J. Zinn-Justin (Plenum, New York, 1980), p. 1.

[3] P. C. Hohenberg, Physica **109& 110B**, 1436 (1982).

[4] V. Dohm and R. Folk, Physica **109& 110B**, 1549 (1982).

[5] V. Dohm and R. Folk, in *Advances in Solid State Physics*, edited by P. Grosse (Vieweg, Braunschweig, 1982), Vol. 22.

[6] J. Kerrisk and W. E. Keller, Bull. Am. Phys. Soc. **12**, 550 (1967); Phys. Rev. **177**, 341 (1969).

[7] J. Kerrisk, Ph.D. thesis, The University of New Mexico, 1968.

[8] R. A. Ferrell, N. Menyhard, H. Schmidt, F. Schwabl, and P. Szepfalusy, Phys. Rev. Lett. **18**, 891 (1967); Phys. Lett. **24A**, 493 (1967); Ann. Phys. (N.Y.) **47**, 565 (1968).

[9] B. I. Halperin and P. C. Hohenberg, Phys. Rev. Lett. **19**, 700 (1967); Phys. Rev. **177**, 952 (1969).

[10] L. Van Hove, Phys. Rev. **93**, 1374 (1954); L. D. Landau and I. M. Khalatnikov, Dokl. Akad. Nauk SSSR **96**, 469 (1954), reprinted in *Collected Papers of L. D. Landau*, edited by D. ter Haar (Pergamon, London, 1965).

[11] M. Archibald, J. M. Mochel, and L. Weaver, Phys. Rev. Lett. **21**, 1156 (1968); in *Proceedings of the Eleventh International Conference on Low Temperature Physics*, edited by J. F. Allen, D. M. Finlayson, and D. M. McCall (University of St. Andrews, St. Andrews, Scotland, 1968), p. 211.

[12] G. Ahlers, Phys. Rev. Lett. **21**, 1159 (1968); in *Proceedings of the Eleventh International Conference on Low Temperature Physics*, Ref. 11, p. 203.

[13] G. Ahlers, in *Proceedings of the Twelfth International Conference on Low Temperature Physics*, edited by E. Kanda (Academic, Tokyo, 1971), p. 21.

[14] B. I. Halperin, P. C. Hohenberg, and E. D. Siggia, Phys. Rev. Lett. **32**, 1289 (1974); Phys. Rev. B **13**, 1299 (1976).

[15] P. C. Hohenberg and B. I. Halperin, Rev. Mod. Phys. **49**, 435 (1977).

[16] K. G. Wilson, Phys. Rev. B **4**, 3174 (1971); **4** 3184 (1971). See also K. G. Wilson and J. Kogut, Phys. Rep. **12C**, 76 (1974); M. E. Fisher, Rev. Mod. Phys. **46**, 597 (1974).

[17] E. D. Siggia, Phys. Rev. B **13**, 3218 (1976).

[18] C. DeDominicis and L. Peliti, Phys. Rev. Lett. **38**, 505 (1977); Phys. Rev. B **18**, 353 (1978).

[19] V. Dohm, Z. Phys. B **31**, 327 (1978).

[20] R. A. Ferrell and J. K. Bhattacharjee, Phys. Rev. Lett. **42**, 1638 (1979); J. Low Temp. Phys. **36**, 165 (1979).

[21] The existence of slow transients and of a narrow critical region also follows from the work of Ferrell and Bhattacharjee (Ref. 20).

[22] P. C. Hohenberg, B. I. Halperin, and D. R. Nelson, Phys. Rev. B **22**, 2372 (1980).

[23] V. Dohm and R. Folk, Z. Phys. B **40**, 79 (1980).

[24] V. Dohm and R. Folk, Phys. Rev. Lett. **46**, 349 (1981).

[25] G. Ahlers, P. C. Hohenberg, and A. Kornblit, Phys. Rev. Lett. **36**, 493 (1981); Phys. Rev. B **25**, 3136 (1982).

[26] V. Dohm and R. Folk, Z. Phys. B **45**, 129 (1981).

[27] V. Dohm and R. Folk, Z. Phys. B **41**, 251 (1981).

[28] W. B. Hanson and J. R. Pellam, Phys. Rev. **95**, 321 (1954).

[29] G. Ahlers, Phys. Rev. Lett. **43**, 1417 (1979).

[30] M. J. Crooks and B. J. Robinson, Phys. Rev. B **27**, 5433 (1983); Physica (Utrecht) **107B**, 339 (1981).

[31] J. A. Tyson, Phys. Rev. Lett. **21**, 1235 (1968). The results of this work are approximately a factor of 5 higher than those of Refs. 29 and 30 and the present data. The agreement between the three recent sets of data, each obtained by a different experimental technique, is a strong indication that Tyson's results are influenced by a systematic error of unknown origin.

[32] R. Mehrotra and G. Ahlers, Phys. Rev. Lett. **51**, 2116 (1983).

[33] R. A. Ferrell and J. K. Bhattacharjee, Phys. Rev. B **24**, 5071 (1981).

[34] R. A. Ferrell and J. K. Bhattacharjee, Phys. Rev. Lett. **51**, 487 (1983).

[35] P. C. Hohenberg (private communication).

[36] G. Ahlers and P. C. Hohenberg, Phys. Rev. Lett. **52**, 313 (1984). For a reply to this Comment, see R. A. Ferrell and J. K. Bhattacharjee, Phys. Rev. Lett. **52**, 314 (1984).

[37] T. Worthington, J. Yan, and J. U. Trefny, J. Low Temp. Phys. **24**, 365 (1976).

[38] M. J. Crooks and B. J. Robinson, Rev. Sci Instrum. **54**, 46 (1983).

[39] See, for instance, G. L. Pollack, Rev. Mod. Phys. **41**, 48 (1969).

[40] H. L. Caswell, Phys. Lett. **10**, 44 (1964).

[41] D. S. Greywall and G. Ahlers, Phys. Rev. A **7**, 2145 (1973); and unpublished.

[42] K. H. Mueller, G. Ahlers, and F. Pobell, Phys. Rev. B **14**, 2096 (1976).

[43] See, for example, R. Truell, C. Elbaum, and B. B. Chick, *Ultrasonic Methods in Solid State Physics* (Academic, New York, 1969), pp. 107—121.

[44] J. Heiserman and I. Rudnick, J. Low Temp. Phys. **22**, 481 (1976), and references therein.

[45] V. Steinberg (private communication).

[46] See, for instance, S. J. Putterman, *Superfluid Hydrodynamics* (American Elsevier, New York, 1974).

[47] V. Dohm (unpublished); in *Proceedings of the Seventeenth International Conference on Low Temperature Physics,* edited by A. Schmid, W. Weber, and H. Wühl (North-Holland, Amsterdam, 1984), p 953.

[48] A. A. Vladimirov, D. I. Kazakov, and O. V. Tarazov, Zh. Eksp. Teor. Fiz. **77**, 1035 (1979) [Sov. Phys.—JETP **50**, 521 (1979)].

[49] A. Singsaas and G. Ahlers, Phys. Rev. B **30**, 5103 (1984).

[50] See, for instance, I. M. Khalatnikov, *Introduction to the Theory of Superfluidity* (Benjamin, New York, 1964).

[51] G. Ahlers, Phys. Rev. A **3**, 696 (1971).

[52] See, for instance, C. Buchal and F. Pobell, Phys. Rev. B **14**, 1103 (1976), and references therein.

[53] C. E. Chase, Proc. R. Soc. London, Ser. A **220**, 116 (1953).

[54] Below 1.8 K, where a comparison is possible, the data for D_1 by J. R. Pellam and C. P. Squire [Phys. Rev. **72**, 1245 (1947)], and by K. Dransfeld, J. A. Newell, and J. Wilks [Proc. R. Soc. London, Ser. A **243**, 500 (1958)], are about 40% higher than those of Chase. If this difference is due to systematic errors in Chase's data, then the difference between $D_2-\lambda'/C_p$ and $(\rho_s/\rho_n)D_1$ may be smaller than shown in Fig. 22 by about 0.5×10^{-4} cm^2/sec.

[55] For a survey of experimental data, see G. Ahlers, Phys. Lett. **37A**, 151 (1971).

[56] See, for instance, I. M. Khalatnikov, in *The Physics of Liquid and Solid Helium,* edited by K. H. Bennemann and J. B. Ketterson (Wiley, New York, 1976), Part I, Chap. 1.